



CrossMark
 click for updates

Cite this: *Soft Matter*, 2016, 12, 2604

Received 30th November 2015,
 Accepted 14th January 2016

DOI: 10.1039/c5sm02906f

www.rsc.org/softmatter

Do Lehmann cholesteric droplets subjected to a temperature gradient rotate as rigid bodies?†

Guilhem Poy* and Patrick Oswald

We performed a Fluorescence Recovery After Photobleaching (FRAP) experiment during the Lehmann rotation of cholesteric droplets in thermodynamic coexistence with the isotropic liquid and subjected to a temperature gradient. By creating and tracking bleached spots near the surface of banded droplets (in which the cholesteric helix is perpendicular to the gradient) and concentric circle droplets oriented by an electric field (in which the helix is parallel to the gradient), we found that neither type of droplet rotates as a solid. This result shows that the texture rotation is mainly due to the local director rotation.

1 Introduction

In 1900, Lehmann¹ observed the rotation of the texture of cholesteric droplets submitted to a temperature gradient. A first theoretical explanation was proposed by Leslie in 1968² who proved that, for symmetry reasons, the director \mathbf{n} in a cholesteric phase experiences a torque proportional to the temperature gradient \mathbf{G} , of expression

$$\Gamma_{\text{Leslie}} = \nu \mathbf{n} \times (\mathbf{n} \times \mathbf{G}). \quad (1)$$

Constant ν is called the Leslie thermomechanical coefficient.

In 2008, the Lehmann experiment was reproduced for the first time with a compensated cholesteric liquid crystal (LC)³ and one year later with a diluted cholesteric mixture.⁴ In these two experiments, the cholesteric phase coexists with the isotropic liquid of the LC and forms droplets with a banded texture, which indicates that the cholesteric helix is perpendicular to the temperature gradient. A simple model, based on the existence of the Leslie torque, allowed one to explain the observed relationship between the measured period of rotation, the size of the droplets and the temperature gradient.³ At this level, it is important to emphasize that this model assumes that there is no flow inside the sample and that the texture rotation is only due to a director rotation induced by Γ_{Leslie} . From these experiments and the model, values of ν were obtained at the melting temperature of the LCs studied. A remarkable point is that the value of ν found in this way is proportional to the equilibrium twist of the phase,⁵ independently of the concentration of

chiral molecules. This last point became obvious when using a compensated mixture in which the compensation temperature coincides with the melting temperature. In that case, the Lehmann rotation disappears in spite of the large concentration of chiral molecules in the mixture.⁶

These results immediately suggested that the Lehmann effect was not due to the Leslie torque, since this torque does not vanish at the compensation temperature as previously shown by observing below the transition temperature the rotation of the director in planar samples treated for sliding anchoring on the two surfaces (Leslie's geometry).^{7,8} This result was reinforced by the fact that the values of ν deduced from the rotation of the droplets are completely different (larger by a factor 10 to 1000) from those obtained in the Leslie's geometry. Even worse, it was shown that the sign of the coefficient could differ between these two techniques. The obvious conclusion is that the coefficient measured from the droplet rotation is not the true Leslie coefficient, but a kind of effective Leslie coefficient, which is now simply called Lehmann coefficient (by opposition to the Leslie thermomechanical coefficient).⁸

In practice, it is also possible to observe droplets with other orientations of the cholesteric helix. For example, Yoshioka *et al.*⁹ observed a coexistence between banded droplets and concentric circle (CC) droplets in which the helix is parallel to the temperature gradient. Similar droplets were also observed in cholesteric mixtures of negative dielectric anisotropy. In these mixtures, CC droplets can be stabilized by applying an AC electric field and can be grown without limit by decreasing the temperature.^{10,11} Droplets with the helical axis tilted with respect to the temperature gradient were also observed recently by Yamamoto *et al.*¹² by using glass plates treated for homeotropic anchoring instead of the sliding planar anchoring.¹³ In all these cases, it was also observed that the director was rotating with an

Université de Lyon, École Normale Supérieure de Lyon, Laboratoire de physique, CNRS, UMR 5672, 46 Allée d'Italie, 69364 Lyon, France.

E-mail: guilhem.poy@ens-lyon.fr

† Electronic supplementary information (ESI) available. See DOI: 10.1039/c5sm02906f

angular velocity much larger than that predicted by the simplified model based on the Leslie explanation.³

In conclusion, there is a large discrepancy between the experiments and the model based on the Leslie explanation. This could mean that the main assumption of the model, namely that there is no flow, is wrong. Indeed, the texture rotation could be explained as well by assuming that the droplets rotate as a rigid body. Such a rotation has already been observed in dye-doped nematic droplets illuminated with a circularly polarized light beam by following the motion of small particles around them.¹⁴ In this case, the electric field of the light exerts an external torque on the droplets which is responsible for their rotation. By contrast, the Leslie torque is internal and, for this reason, cannot exert a net torque on the droplet.¹⁰ In other words, another mechanism than the Leslie torque must be found for explaining a solid rotation of the droplets, if it exists.

Before starting to look for this new mechanism, it is thus crucial to determine if the droplets rotate as rigid bodies, or if their texture rotation is only due to an individual rotation of the director without flow, as assumed so far in the model. This is the goal of this paper.

This question was already raised by Yoshioka *et al.*⁹ who used a photobleaching technique to discriminate between these two types of rotation. In their experiment, the LC is doped with a fluorescent dye. With a laser, a bleached spot is created inside a droplet, the evolution of which is followed in fluorescence microscopy. The existence of a flow is determined by observing the motion of the spot center when the spot is diffusing. Their conclusion was that the banded droplets rotate as a rigid body, whereas in the CC droplets, only the director is rotating (no flow).

Given the importance of these results, we decided to perform again this experiment while changing strategy.

Indeed, one of the main difficulties in the experiment of Yoshioka *et al.* is to precisely determine the position of the spot center. This is very difficult in banded droplets because the bands remain visible in fluorescence microscopy, which modulates the spot intensity. To avoid this difficulty, we chose to bleach a spot nearby the droplet, in the isotropic liquid, and to follow its time evolution by only analyzing the fluorescence signal outside the droplet. If the droplets are rotating as found by Yoshioka *et al.*, a flow should exist outside the droplet near its surface, and the spot should be advected and stretched by this flow.

In the case of CC droplets on the contrary, our spot was created inside the droplet as Yoshioka *et al.* did, but we used in our case a liquid crystal of negative dielectric anisotropy with a very small birefringence. This offered us the double advantage of being able to orient the droplets under an electric field while making the internal texture of the droplet almost invisible in fluorescence microscopy.

In addition, we chose cholesteric mixtures in which the droplets rotate very fast in order to be able to follow the spot during at least a half-revolution. This is much more than in the experiment of Yoshioka *et al.* where the droplets were only rotating by 10–30° during the measurements.

2 Experimental procedure

The two-ovens experimental setup and the procedure used to observe the Lehmann effect have already been described in a previous paper.³ Briefly, each sample is constituted of two glass plates (covered with an ITO layer when an electric field is required) separated by nickel wires of calibrated diameter. These two plates are covered by a 20 nm thick polymercaptan layer, which ensures a planar sliding anchoring. The sample thickness h is measured with a spectrometer to within $\pm 0.1 \mu\text{m}$ before each experiment. This sample is filled with the studied liquid crystal mixture: 7CB (4,4'-*n*-heptyl-cyanobiphenyl, Frinton Laboratories) or CCN37 (4 α ,4' α -propylheptyl-1 α ,1' α -bicyclohexyl-4 β -carbonitriles, Nematel), doped with a mass fraction C of the chiral molecule R811 (*R*-[+]-octan-2-yl 4-[[4-(hexyloxy)benzoyl]-oxy]benzoate, Merck) and a mass fraction of 0.05 wt% of the fluorescent dye NBD C6-ceramide (*N*-[2-hydroxy-1-(hydroxymethyl)-3-heptadecenyl]-6-[[7-nitro-2,1,3-benzoxadiazol-4-yl]amino], Interchim). This dye is interesting for two reasons: it has a good quantum yield which allows working with very small concentrations of dye and, more important, it is easily bleached by the laser, which avoids to heat the sample and melt the droplet during the laser shot, a problem we met when we used more classical dyes such as the Nile Red or the DiA dyes. Once filled, the sample is then sandwiched between two ovens regulated to within $\pm 1/100 \text{ }^\circ\text{C}$. Two very thin layers of glycerol ensure a good thermal contact between the sample and the ovens. It has already been shown³ that the temperature gradient G inside the sample is proportional to both the difference of temperature $\Delta T = T_+ - T_-$ between the two ovens and the ratio of thermal conductivities in the glass and the LC, and depends very little on the sample thickness. This stems from the fact that the layer of LC is very thin compared to the glass plates. In the experiments with the banded droplets (respectively, with the CC droplets), we applied $\Delta T = -10 \text{ }^\circ\text{C}$ (respectively, $-5 \text{ }^\circ\text{C}$), which corresponds to $G = -18 \text{ mK } \mu\text{m}^{-1}$ (respectively, $G = -9 \text{ mK } \mu\text{m}^{-1}$).

Fig. 1 schematizes the entire setup, constituted of three parts. The middle part is formed by the two ovens and the sample. The upper part is designed to visualize the signal of fluorescence of the sample in reflection. It includes a mercury-vapor lamp illuminating the sample in reflection and a CCD camera (C4742, Hamamatsu) collecting the fluorescence signal through a microscope objective ($\times 10$). The fluorescence filter cube I3 (Leica Microsystems) selects on the input the excitation signal ($\lambda = 450\text{--}490 \text{ nm}$) and on the output the fluorescence emission signal only ($\lambda \geq 515 \text{ nm}$).

The lower part is designed to easily create bleached spots in the sample, based on the technique of Fluorescence Recovery After Photobleaching (FRAP). A solid state laser (Sapphire SF 488-100 CW CDRH, Coherent) creates a Gaussian beam (wavelength $\lambda = 488 \text{ nm}$), which is then cleaned by a spatial filter and focused onto the sample thanks to the condenser of the microscope of focal length 1 cm. A custom-built shutter (S1) allows setting the duration of the exposure to the Laser beam, while another shutter (S2) protects the camera during the exposure. In all experiments, the shot duration is 40 ms and the laser power is 10 mW. The shutter S1 can also be replaced

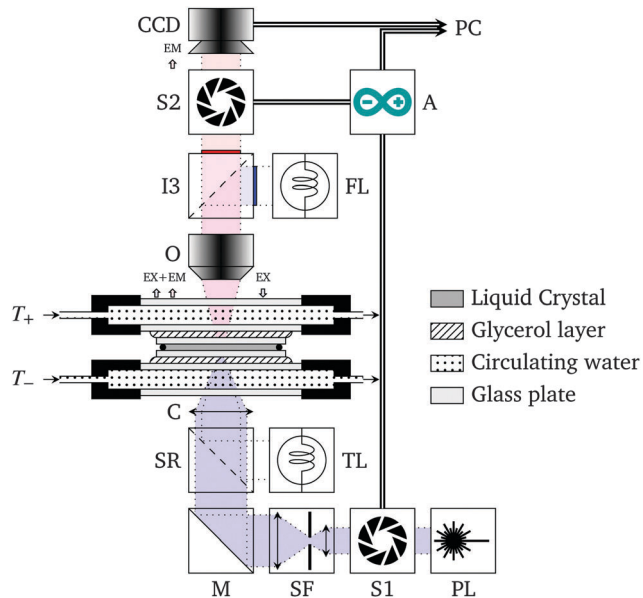


Fig. 1 The setup used for the FRAP experiment. The sample is observed in reflection with the mercury-vapor lamp FL, the objective O, and the CCD camera. The filter cube I3 allows us to only illuminate the sample with the excitation signal EX and to filter out the reflected signal EX to keep only the emission signal EM of the dye. Bleached spots are created by focusing the Gaussian beam of the laser PL with the condenser C onto the sample, after it has been cleaned by the spatial filter SF. The exposure duration is set by two DIY shutters S1 and S2 controlled by the arduino A (S2 protects the camera during the exposure). Finally, the lamp TL and the semi-reflective plate SR allow us to observe the sample in transmission with natural light. For clarity, the absorptive filter, the polarizers and the translation stages are not represented.

by an absorptive filter which allows observing the spot directly with the camera. In this way, the spot size and its position on the screen of the camera can be finely tuned. The two shutters and the absorptive filter are piloted with an Arduino. The camera and the Arduino are interfaced with a Labview program. Finally, the two ovens and the sample can be moved thanks to two translation stages in order to accurately position the sample with respect to the spot. In addition, a halogen lamp and a semi-reflective plate allow observing the sample in transmission (between crossed polarizers when necessary) with natural light. With this system, it is very easy to bleach the sample in the vicinity of any droplet and follow the later evolution of the bleached spot.

3 Photobleaching in banded droplets

In this section, we present and discuss the results obtained with the banded droplets, first in a mixture of 7CB doped with 0.05 wt% of the fluorescent dye and $C = 0.25$ wt% of R811 and then in mixtures more concentrated in R811. This first concentration was not chosen randomly but in order to maximize the ratio velocity/size when the droplets have a typical diameter of 50–100 μm .¹¹ In a sample of thickness $h = 21$ μm , we created a bleached spot near a droplet of radius $R = 43$ μm rotating at angular velocity $\omega_{\perp} = 0.139$ rad s^{-1} . Fig. 2 shows this droplet in

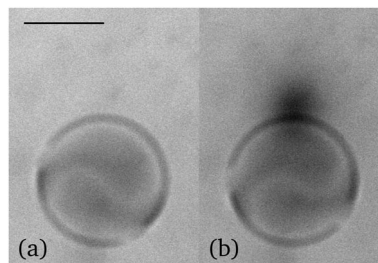


Fig. 2 Two raw fluorescence images of a cholesteric droplet coexisting with its isotropic liquid taken before (a) and after (b) a laser shot near the droplet surface. Mixture of 7CB + 0.25 wt% R811 + 0.05 wt% NBD C6-ceramide $h = 21$ μm . The black bar represents 50 μm .

fluorescence microscopy just before the shot (photo (a)) and immediately after the spot was created (photo (b)). A first observation is that the background is darker in photo (b) than in photo (a). This is due to the natural photobleaching of the fluorescent dye by the mercury-vapor lamp. A second observation is that this natural photobleaching is not perfectly uniform over the image. This comes from the fact that the lighting is not perfectly uniform too. In practice, we want to only detect the fluorescence signal coming from the spot, and so we need to eliminate all the signal coming from the natural photobleaching and the non-uniformity of the lighting. To do so, we solved the diffusion/advection equation for the dye density by taking into account the destruction term coming from the photobleaching and found an estimate for the only contribution of the bleached spot (renormalized to 1 at time $t = 0$):

$$\hat{s}(\mathbf{x}, t) = \frac{I(\mathbf{x}, t) - I_0}{I(\mathbf{x}, 0) - I_0} e^{\alpha[I(\mathbf{x}, 0) - I_0]t}. \quad (2)$$

In this equation, $I(\mathbf{x}, t)$ represents the intensity at point \mathbf{x} and time t in an image of the acquisition stack, I_0 is an average of the additive noise introduced by the camera, and α is the rate of destruction of the dye per unit of light intensity. Time $t = 0$ is chosen just before the laser shot when there is no bleached spot. We refer to the Appendix for the complete demonstration of this formula. Note that, by definition, \hat{s} is approximately equal to 1 far from the bleached spot and is strictly less than 1 inside. For each acquisition, the value of the rate of destruction α is obtained from a linear regression *versus* time of the quantity

$$\frac{1}{I(\mathbf{x}, 0) - I_0} \ln \left[\frac{I(\mathbf{x}, t) - I_0}{I(\mathbf{x}, 0) - I_0} \right] \quad (3)$$

measured in the isotropic liquid far from the bleached spot, where we impose $\hat{s} \simeq 1$.

Finally, note that the expression of \hat{s} is only valid in the isotropic liquid and not inside the droplet. This stems from the fact that the fluorescence intensity inside the droplet depends on the orientation of the bands, and so would change over time at each point even when there is no photobleaching. This additional phenomenon, certainly due to the variation of the optical index along the helical axis, is not taken into account in our analysis, which only applies for a constant optical index.

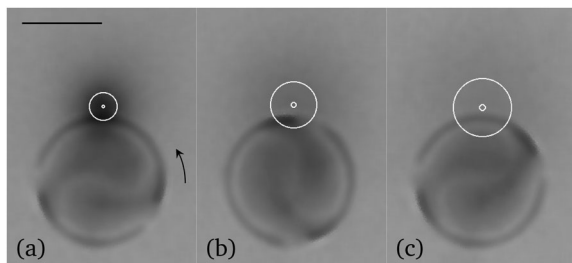


Fig. 3 Image representations (smoothed by an adaptive Wiener filter) of the estimate \hat{s} computed from the droplet of Fig. 2 for $\Delta t = 0.5$ s (a), 11.726 s (b) and 23.064 s (c). The droplet is rotating counterclockwise at angular velocity $\omega_{\perp} = 0.139$ rad s^{-1} when $\Delta T = -10$ °C. The white dot represents the center of the fitted Gaussian function, and the white circle represents the circle of equation $|\mathbf{x} - \mathbf{x}_0| = \sigma/2$. The black bar represents 50 μm .

For this reason, the spot analysis will be conducted by taking into account only the intensity measured outside the droplet. In the following, we shall display \hat{s} as an image by using an effective \hat{s} inside the droplet. The latter is obtained by replacing $[I(\mathbf{x}, 0) - I_0]$ in eqn (2) by a linear regression of the same quantity outside the droplet. This choice is arbitrary but allows us to see the bands and their rotation inside the droplet. This is visible in Fig. 3 where the function \hat{s} corresponding to the droplet shown in Fig. 2 is represented at three different $\Delta t = t - t_{\text{shot}}$ (by denoting by t_{shot} the time at the end of the laser shot). Note that in our experiment Δt is always ≥ 0.5 s because our homemade camera shutter opens half a second after the end of the shot. We also mention that, for viewing comfort, an adaptive Wiener filter has been used to smooth the images of \hat{s} in Fig. 3. However, all analyses were conducted on the raw signal. These images show that the effect of the natural photobleaching is well corrected by the exponential factor in the expression of \hat{s} .

We now turn to the quantitative analysis of these images. Our goal is to determine whether or not the bleached spot is dragged by the droplet when it rotates. A rapid visual examination of the Movie M1 in the ESI† shows that the spot seems to not move.

To confirm this result, we fitted the raw signal $\hat{s}(\mathbf{x}, t)$ with the Gaussian function

$$s_g(\mathbf{x}, t) = s_0(t) + \Delta s(t) \exp\left\{-\frac{[\mathbf{x} - \mathbf{x}_0(t)]^2}{2\sigma(t)^2}\right\}. \quad (4)$$

The center $\mathbf{x}_0(t)$ and the half-variance $\sigma(t)$ were obtained by using a Levenberg–Marquardt regression algorithm. This non-linear regression was applied by choosing a Region of Interest (ROI) around the bleached spot and by eliminating all points inside both the droplet and the ROI. The remaining points were then processed by the Levenberg–Marquardt algorithm, which allowed us to determine the Gaussian parameters s_0 , Δs , \mathbf{x}_0 and σ as functions of time. The two important parameters are the spot center \mathbf{x}_0 marked by a white dot in Fig. 3 and the half-variance $\sigma/2$ represented by the white circle of equation $|\mathbf{x} - \mathbf{x}_0| = \sigma/2$ in the same figure. These two elements are also shown in the Movie M1 of the ESI.†

Before commenting these results, we still need to test the validity and the accuracy of the fits. Indeed, a visual check is clearly insufficient, in particular at the end of the recording when the signal becomes very weak. For this reason and for making the comparison between the fit and the raw data more quantitative, we compared two polar marginal distributions calculated from \hat{s} and s_g . In the case of \hat{s} , these distributions are defined as follows:

$$\hat{g}_r(r, t) = \frac{1}{\pi} \int_0^{\pi} \hat{s}(r, \theta, t) d\theta, \quad (5)$$

$$\hat{g}_{\theta}(\theta, t) = \frac{1}{R_{\text{tot}}} \int_0^{R_{\text{tot}}} \hat{s}(r, \theta, t) dr, \quad (6)$$

where the polar referential $\{r, \theta\}$ is centered on the fitted center of the spot \mathbf{x}_0 at each time t . So defined, \hat{g}_r can be interpreted as the mean radial profile inside the upper half-space (where the spot does not overlap with the droplet) while \hat{g}_{θ} can be seen as a mean angular profile inside an upper half-disc of radius R_{tot} . In the calculation, the value of R_{tot} is chosen to be of the same size as the regression ROI, which is always $\geq 3\sigma(t)$. These two integrals are numerically calculated by discretizing the integration intervals and by evaluating \hat{s} at each point with a bilinear interpolation.

In a similar way, the two marginal distributions for the Gaussian model s_g are defined as:

$$g_r(r, t) = \frac{1}{\pi} \int_0^{\pi} s_g(r, \theta, t) d\theta = s_0(t) + \Delta s(t) \exp\left[-\frac{r^2}{2\sigma(t)^2}\right], \quad (7)$$

$$g_{\theta}(\theta, t) = \frac{1}{R_{\text{tot}}} \int_0^{R_{\text{tot}}} s_g(r, \theta, t) dr \\ \simeq s_0(t) + \Delta s(t) \frac{\sigma(t)}{R_{\text{tot}}} \sqrt{\frac{\pi}{2}}. \quad (8)$$

The expression of g_{θ} follows from $\text{erf}[R_{\text{tot}}/(\sqrt{2}\sigma)] \simeq 1$ as long as $R_{\text{tot}} \geq 3\sigma$.

From these definitions, it comes immediately that, in the ideal case of an axisymmetric Gaussian function (as defined in eqn (4)), $g_r(r, t)$ is a 1D Gaussian profile which flattens in time, while $g_{\theta}(\theta, t)$ is independent of θ and decreases as time elapses. By contrast, $\hat{g}_{\theta}(\theta, t)$ should depend on θ if the profile is no longer axisymmetric. This could be the case experimentally, whence the interest of this function to test the axisymmetry of the experimental spot. The interpretation of the functions \hat{g}_{θ} and g_{θ} is still more transparent when the following definitions of the local variance are used:

$$\hat{\sigma}(\theta, t) = R_{\text{tot}} \left[\frac{\hat{g}_{\theta}(\theta, t) - s_0(t)}{\Delta s(t)} \right] \sqrt{\frac{2}{\pi}}, \quad (9)$$

$$\sigma(\theta, t) = R_{\text{tot}} \left[\frac{g_{\theta}(\theta, t) - s_0(t)}{\Delta s(t)} \right] \sqrt{\frac{2}{\pi}} \equiv \sigma(t). \quad (10)$$

These are the functions that we calculated together with the functions \hat{g}_r and g_r . They are plotted in Fig. 4. Concerning the experimental radial profile \hat{g}_r , we see that, although it is not

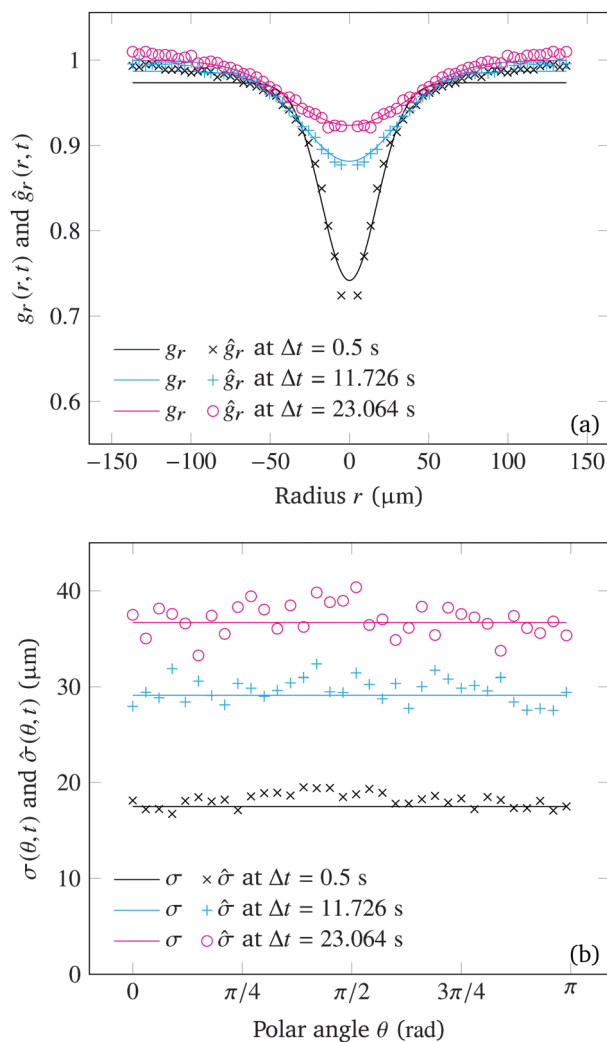


Fig. 4 Comparison between the radial (a) and the variance (b) profiles of the data \hat{s} of Fig. 3 (markers) and the Gaussian fit s_g (lines) at three different Δt . Note that the radial profiles have been symmetrized around 0 for a better visualization.

perfectly Gaussian at the beginning, it very quickly relaxes towards the fitted Gaussian profile g_r . As for the experimental variance profile $\hat{\sigma}$, it is quite flat and equal in average to the fitted value of the variance σ , even at the end of the recording. This proves that the spot stays axisymmetric. These results validate our method of analysis of the experimental results.

We can now assert that the center of the bleached spot does not move within our precision, in spite of the fact that the droplet rotates one-half turn. More precisely, the spot center has an erratic motion and does not move further than $3.5 \mu\text{m}$ from its initial position during the complete acquisition. In addition, and this is crucial in our analysis, the spot remains axisymmetric as it should be in a fluid at rest. These results show that there is no detectable flow outside the droplet. This suggests that the droplet does not rotate as a solid, because we should detect a flow if it was the case. Indeed, a solid rotation would imply a non-zero velocity at the surface of the droplet, creating a shear flow inside the isotropic liquid over a distance

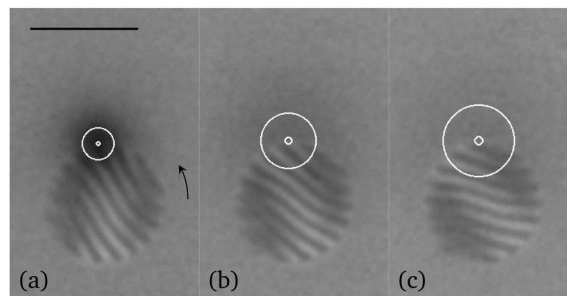


Fig. 5 The same as in Fig. 3 with a droplet more distorted of radius $R = 28 \mu\text{m}$, rotating counterclockwise at angular velocity $\omega_{\perp} = 0.036 \text{ rad s}^{-1}$ when $\Delta T = -10 \text{ }^{\circ}\text{C}$. $\Delta t = 0.5$ s (a), 10.281 s (b) and 20.174 s (c). Mixture of 7CB + 0.63%R811 + 0.05%NBD C6-ceramide. The black bar represents $50 \mu\text{m}$.

of the order of the droplet radius R when $2R < h$ (in this case, the droplet is spherical¹²) and of the order of h when $2R > h$ (as in our case). This flow should advect and deform the spot in a visible way, which we do not detect.

Our results are thus in disagreement with the findings of Yoshioka *et al.*⁹ Nevertheless a careful reader could object that in our experiment the director field inside the droplet is much less distorted than in the case of Yoshioka *et al.* where the number of bands is larger (8 instead of 1 here). To test whether this difference could explain the disagreement between the two experiments, we performed additional measurements with mixtures more concentrated in R811 and again reached the conclusion that there is no visible flow outside the droplets whatever the number of bands and their assembly inside. To illustrate this point, an example of a droplet quite similar to that studied by Yoshioka *et al.* is shown in Fig. 5 and in the Movie M2 of the ESI.† In this new experiment, the concentration of R811 is $C = 0.63 \text{ wt}\%$, the droplet radius is $R = 28 \mu\text{m}$, the number of bands is equal to 8 and the droplet rotates by ~ 40 degree during the acquisition time (≈ 20 second). The same analysis as before shows that the spot center is immobile (more precisely, it has an erratic trajectory and does not move further than $2.4 \mu\text{m}$). In addition, the spot remains axisymmetric as shown in Fig. 6 which indicates that there is no visible flow outside the droplet.

Our conclusion is that the banded droplets do not rotate as a solid, regardless of the number of bands inside. The contradiction with the conclusion of Yoshioka *et al.*⁹ is perhaps due to an artifact in their measurements that are particularly difficult to interpret when the spot is created inside the droplet.

4 Photobleaching in oriented CC droplets

In this Section, we extend our experiments to the case of CC droplets in which the cholesteric helix is parallel to the temperature gradient. Contrary to Yoshioka *et al.*, we used a LC with a negative dielectric anisotropic, which offers the advantage of being able to orient the helix with an electric field in all the droplets, whatever their size. This allowed us to prepare CC

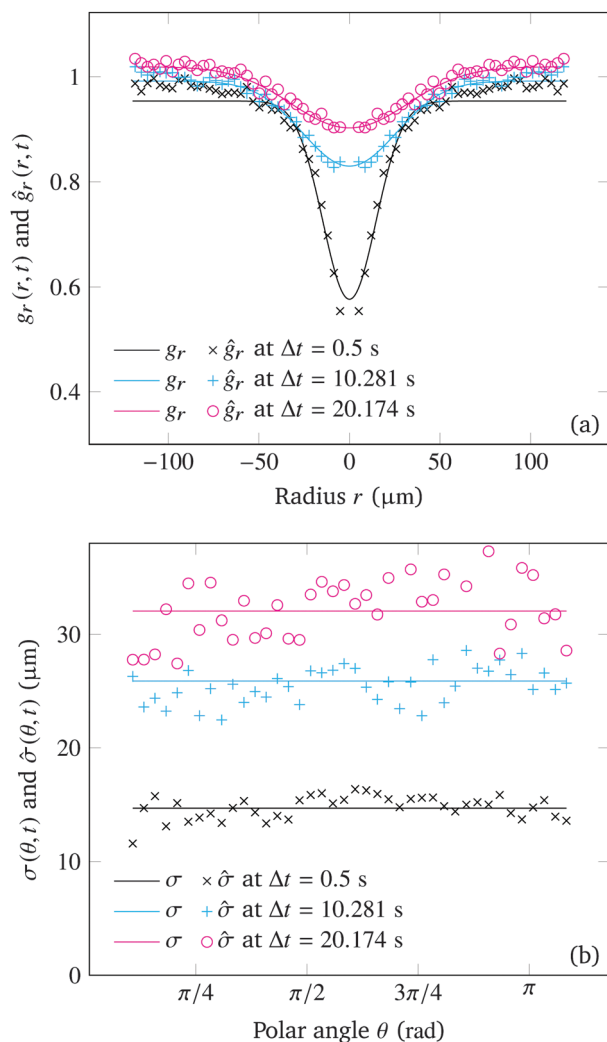


Fig. 6 The same as in Fig. 4 for the droplet shown in Fig. 5.

droplets much bigger than the size of the laser spot. In addition, we chose a LC with a very small birefringence in order that the CC texture observable in transmission between crossed polarizers becomes almost invisible in fluorescence microscopy. Thanks to this, it is possible to shoot inside the droplets and to analyze the bleached spot with the same tools as in the previous section. As for the angular velocity of the helix ω_{\parallel} , it is measured by observing the droplet in transmission between crossed polarizers just before the shot.

In practice, we used a mixture of CCN37 doped with 0.05 wt% of the fluorescent dye NBD C6-ceramide and $C = 2.6$ wt% of the chiral molecule R811. The birefringence of CCN37 is very small,¹⁵ of the order of 2×10^{-2} . The reader will note the high concentration of R811 used in this experiment. This is to increase the angular velocity of the texture which we know to be proportional to C in this type of droplets.^{10,11}

Fig. 7 shows an oriented CC droplet of radius $R = 69 \mu\text{m}$ rotating at angular velocity $\omega_{\parallel} = 0.24 \text{ rad s}^{-1}$ when $\Delta T = -5 \text{ }^{\circ}\text{C}$. The sample thickness is $h = 22.6 \mu\text{m}$. An AC electric field (10 Vrms, 10 kHz) was used to orient this droplet. As the optical

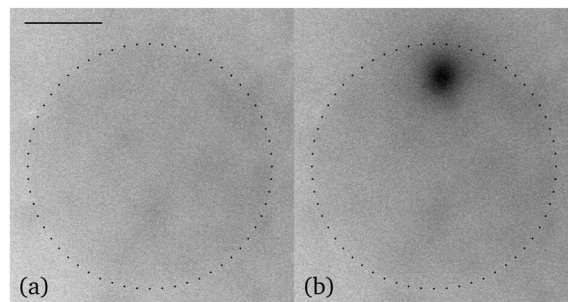


Fig. 7 Two raw fluorescence images of a CC droplet coexisting with its isotropic liquid taken before (a) and after (b) a laser shot inside the droplet. An electric field is applied in order to orient the helix parallel to the temperature gradient. The dotted circle marks the boundary of the droplet, barely visible because of the small birefringence of the LC. Mixture of CCN37 + 2.6 wt% R811 + 0.05 wt% NBD C6-ceramide $h = 22.6 \mu\text{m}$. The black bar represents $50 \mu\text{m}$.

indices are almost the same in the cholesteric phase and the isotropic liquid, the droplet is barely visible in fluorescence microscopy. This is the reason why its boundary is marked with a dotted circle in Fig. 7. Photo (a) shows the raw fluorescence image of the droplet just before the shot and photo (b) just after the shot (0.5 s later).

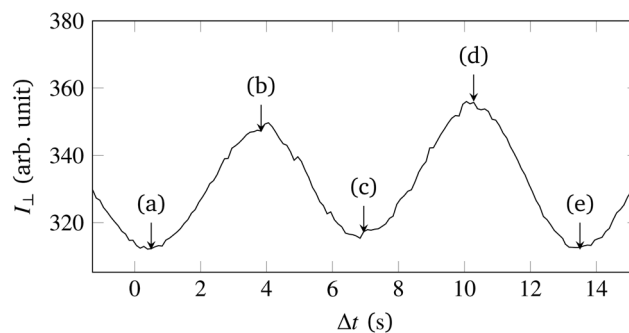
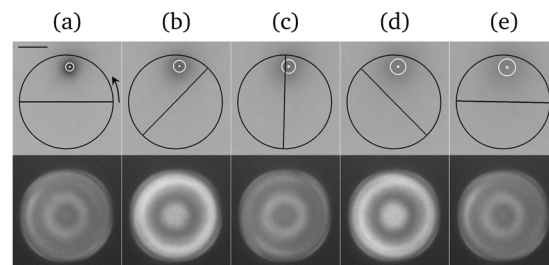


Fig. 8 Evolution of the bleached spot inside the droplet of Fig. 7. Images in the top row show a representation of \hat{s} smoothed by a Wiener filter. The white dot represents the fitted spot center \mathbf{x}_0 and the white circle represents the circle of equation $|\mathbf{x} - \mathbf{x}_0| = \sigma/2$. The droplet boundary is marked by a black circle. The black line gives the helix orientation at the center of the droplet (to within an unknown angle). Images have been taken at times $\Delta t = 0.5 \text{ s}$ (a), 3.8 s (b), 6.9 s (c), 10.3 s (d) and 13.5 s (e). The black bar in the corner of (a) represents $50 \mu\text{m}$. The photos in the second row show the same droplet before the shot observed in transmission between crossed polarizers at similar interval of times. The graph shows the intensity I_{\perp} measured in the center of the droplet. From this graph the texture rotation velocity is deduced: $\omega_{\parallel} = 0.24 \text{ rad s}^{-1}$.

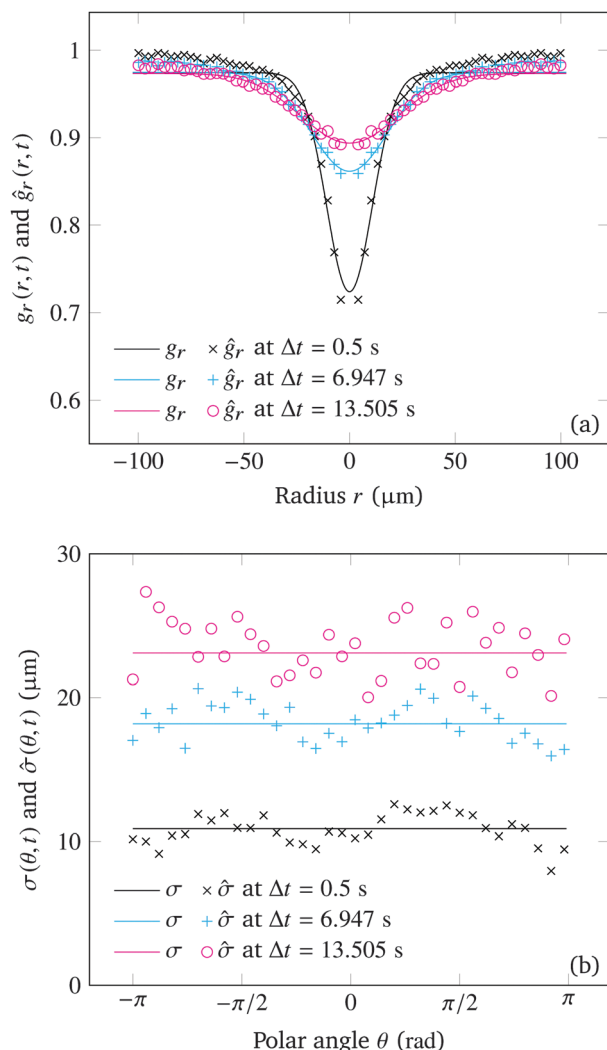


Fig. 9 Comparison of the radial (a) and variance (b) profiles of the data \hat{s} (markers) and Gaussian model s_g (lines) at three different Δt . As before, the radial profiles has been symmetrized around $r = 0$.

In order to detect a possible flow inside the droplet, we calculated as a function of time the signal \hat{s} of the bleached spot inside the droplet, which is possible because of the very small birefringence. This signal is represented as an image in Fig. 8 at five different Δt (see also the Movie M3 of the ESI[†]). As before, a Wiener filter has been used to smooth the images, but all analyses were conducted on the raw signal \hat{s} . As the calculation of \hat{s} keeps only the contribution of the bleached spot, the droplet becomes completely invisible in these images. This is why the droplet boundary was emphasized by a black circle. Images of the same droplet taken before the shot in transmission between crossed polarizers and a plot of the intensity measured in the center of the droplet are also shown in Fig. 8. These images show that the helix, the orientation of which is represented by a black bar in the images of the top row, rotates by 180° during the recording. As before, the white dot and the white circle represent respectively the center and the half-variance of the Gaussian fit function s_g . These two elements are also shown in the Movie M3 of the ESI[†].

Finally, we checked again that there was a good agreement between the fit and the data. To this end, we used the variance profiles defined before $\{\sigma(\theta,t), \hat{\sigma}(\theta,t)\}$ and a slightly modified definition of the radial profiles $\{g_r(r,t), \hat{g}_r(r,t)\}$:

$$g_r(r,t) = \frac{1}{2\pi} \int_0^{2\pi} s_g(r,\theta,t) d\theta, \quad (11)$$

$$\hat{g}_r(r,t) = \frac{1}{2\pi} \int_0^{2\pi} \hat{s}(r,\theta,t) d\theta, \quad (12)$$

where the integration in θ is now done over the whole interval $[0, 2\pi]$ as the spot lies inside the droplet.

The radial and variance profiles are shown in Fig. 9. Again, we observe that the spot is not perfectly Gaussian just after the shot, but relaxes very quickly towards a Gaussian profile. Although the variance profiles are more noisy than previously and seem to show a slight anisotropy, the standard deviation of $\hat{\sigma}$ always corresponds to $\sim 10\%$ of the mean variance σ at each time, which indicates that the spot globally conserves its shape.

In conclusion, we see that the bleached spot is again well fitted by an axisymmetric Gaussian function till the end of the recording. This analysis and the results shown in Fig. 8 and in the Movie M3 of the ESI[†] indicate that the spot center does not move significantly (it does not move further than $1.3 \mu\text{m}$ from its initial position and its trajectory is erratic).

We can thus conclude that there is no measurable flow inside the CC droplets and that the texture rotation is only due to a local rotation of the director. This result is in agreement with the results of Yoshioka *et al.* We mention that we also checked that there is no flow outside the droplets.

5 Conclusion

The photobleaching experiment shows that there is no visible flow outside the banded droplets as well as inside and outside the CC droplets. These results are in agreement with the results of Yoshioka *et al.* for the CC droplets. By contrast, the absence of flow outside the banded droplets seems incompatible with the conclusions of Yoshioka *et al.*, namely that the banded droplets rotate as a rigid body (barycentric rotation). We did not try to follow ourselves the evolution of a bleached spot inside a banded drop because the analysis is very complicated. Subtract the band contrast while taking into account the anisotropic diffusion of the dye inside the droplet is indeed very difficult and neglecting these effects could lead to artifacts. A best method could be to follow the motion of an individual dye molecule inside the droplet.¹⁶ Such an experiment is planned in the future.

It, of course, remains to understand the physical origin of this director rotation. But one thing is certain: it is not due to the Leslie thermomechanical coupling, of microscopic origin whereas the Lehmann effect is clearly of macroscopic origin as we recalled in the Introduction. The solution could be in the complete resolution of the equations of the nematodynamics (including the thermal diffusion equation for the temperature field), without introduction of the Leslie terms, as L. Kramer suggested before he died in a paper never published.

Appendix: estimation of the bleached spot signal

In this appendix, we show how to process the raw images recorded experimentally in order to extract the only contribution from the bleached spot. Indeed, due to the natural photobleaching by the mercury-vapor lamp, the non-uniform background of the image (typical variation of 5–15% inside the ROI) has a non-trivial time evolution. We represent the recorded images (acquisition stack) by a function $I(\mathbf{x}, t)$, where \mathbf{x} is the position of a point in the image and t is the acquisition time of the image. As this stack corresponds to a fluorescence signal, we suppose that

$$I(\mathbf{x}, t) = [1 - \chi_{[t_1, t_2]}(t)] f_{\text{FL}}(\mathbf{x}) n(\mathbf{x}, t) + b(\mathbf{x}, t), \quad (13)$$

where $f_{\text{FL}}(\mathbf{x})$ represents the received light intensity of the lamp (not perfectly uniform) at \mathbf{x} , $n(\mathbf{x}, t)$ is the normalized dye density such that $n(\mathbf{x}, 0) = 1$, and $b(\mathbf{x}, t)$ is the additive noise introduced by the camera. Function $\chi_{[t_1, t_2]}$ is the indicator function of the time interval $[t_1, t_2]$ during which the laser shutter is open and the camera shutter is closed. I and b are without unit, but depend of the settings of the camera. In all our experiments, we worked in 12 bits mode, such that the mean and the standard deviation of the noise are respectively $I_0 \equiv \mathbb{E}(b) \simeq 201.4$ and $\text{std}(b) \simeq 3.120$, and the maximum value measurable by the camera is 4096. Here, \mathbb{E} is the mathematical expectation, estimated with an arithmetic mean of a statistical sample, and the standard deviation is defined as $\text{std}(b) = [\mathbb{E}(b^2) - \mathbb{E}(b)^2]^{1/2}$.

The dye density n must satisfy the equation of diffusion/advection, with an additional destruction term corresponding to the photobleaching:

$$\frac{dn}{dt} = D\nabla^2 n - \alpha(f_{\text{FL}} + \chi_{[t_1, t_2]} f_{\text{PL}})n, \quad (14)$$

where $d/dt = \partial/\partial t + \mathbf{v} \cdot \nabla$ is the advective derivative, D is the diffusion coefficient of the dye in the liquid crystal, α is the destruction rate of the dye, and f_{FL} (respectively f_{PL}) represents the local intensity received from the lamp (respectively from the laser). Looking for a solution of eqn (14) in the form:

$$n(\mathbf{x}, t) = s(\mathbf{x}, t) e^{-\alpha f_{\text{FL}}(\mathbf{x}) t}, \quad (15)$$

yields the following equation for s :

$$\frac{ds}{dt} - \frac{s}{\tau} = D(\nabla^2 s - k^2 s) - \alpha \chi_{[t_1, t_2]} f_{\text{PL}} s, \quad (16)$$

where $1/\tau = \alpha t(\mathbf{v} \cdot \nabla) f_{\text{FL}}$ and $k^2 = \alpha t - \nabla^2 f_{\text{FL}} - (\alpha t \nabla f_{\text{FL}})^2$.

The value of α can be obtained from an acquisition without laser shot in an isotropic region, which typically gives $\alpha \simeq 2 \times 10^{-4} \text{ s}^{-1}$. In addition, as $f_{\text{FL}}(\mathbf{x})$ represents a nearly – but not perfectly – uniform background, we can assume that $|\nabla f_{\text{FL}}| \ll |\nabla s|$. As a consequence, we can neglect in eqn (16) the two terms proportional to s/τ and $k^2 s$ for a typical experiment duration of 30 s. We can therefore write the final equation for s :

$$\frac{ds}{dt} = D\nabla^2 s - \alpha \chi_{[t_1, t_2]} f_{\text{PL}} s. \quad (17)$$

This equation is similar to eqn (14) without f_{FL} . For this reason, it approximates an ideal situation where the lamp would not kill the fluorescence. We can therefore interpret s as the contribution of the bleached spot to the fluorescence signal and $\exp[-\alpha f_{\text{FL}}(\mathbf{x}) t]$ as the contribution of the non-uniform background, slowly decreasing because of the natural photobleaching by the mercury-vapor lamp.

Experimentally, we only know $I(\mathbf{x}, t)$ and α . To estimate s , we note that we can write a relation between s and I :

$$s(\mathbf{x}, t) = \frac{\mathbb{E}[I(\mathbf{x}, t)] - I_0}{\mathbb{E}[I(\mathbf{x}, 0)] - I_0} e^{\alpha[\mathbb{E}[I(\mathbf{x}, 0)] - I_0] t}, \quad (18)$$

which follows from the fact that $n(\mathbf{x}, 0) = 1$. We then deduce the most simple estimate \hat{s} of s by replacing $\mathbb{E}(I)$ by I (a valid approximation, since the standard deviation of the noise is negligible compared to $I - I_0$):

$$\hat{s}(\mathbf{x}, t) = \frac{I(\mathbf{x}, t) - I_0}{I(\mathbf{x}, 0) - I_0} e^{\alpha[I(\mathbf{x}, 0) - I_0] t}, \quad (19)$$

As explained in the body text, this formula is not valid inside the banded droplets. On the other hand, it applies outside of the banded droplet and inside (and outside) the CC droplets.

References

- 1 O. Lehmann, *Ann. Phys.*, 1900, **307**, 649–705.
- 2 F. M. Leslie, *Proc. R. Soc. A*, 1968, **307**, 359–372.
- 3 P. Oswald and A. Dequidt, *Phys. Rev. Lett.*, 2008, **100**, 217802.
- 4 P. Oswald, *Eur. Phys. J. E: Soft Matter Biol. Phys.*, 2009, **28**, 377–383.
- 5 P. Oswald, L. Jørgensen and A. Żywociński, *Liq. Cryst.*, 2011, **38**, 601–613.
- 6 P. Oswald, *Eur. Phys. J. E: Soft Matter Biol. Phys.*, 2012, **35**, 1–17.
- 7 P. Oswald and A. Dequidt, *Europhys. Lett.*, 2008, **83**, 16005.
- 8 P. Oswald, *Europhys. Lett.*, 2014, **108**, 36001.
- 9 J. Yoshioka, F. Ito, Y. Suzuki, H. Takahashi, H. Takizawa and Y. Tabe, *Soft Matter*, 2014, **10**, 5869–5877.
- 10 P. Oswald and S. Pirkel, *Phys. Rev. E: Stat., Nonlinear, Soft Matter Phys.*, 2014, **89**, 022509.
- 11 P. Oswald and G. Poy, *Phys. Rev. E: Stat., Nonlinear, Soft Matter Phys.*, 2015, **91**, 032502.
- 12 T. Yamamoto, M. Kuroda and M. Sano, *Europhys. Lett.*, 2015, **109**, 46001.
- 13 P. Oswald, A. Dequidt and A. Żywociński, *Phys. Rev. E: Stat., Nonlinear, Soft Matter Phys.*, 2008, **77**, 061703.
- 14 C. Manzo, D. Paparo, L. Marrucci and I. Jánossy, *Phys. Rev. E: Stat., Nonlinear, Soft Matter Phys.*, 2006, **73**, 051707.
- 15 B. S. Scheuble, G. Weber and R. Eidenschink, *Proc. Eurodisplay 84 (Paris)*, 1984, pp. 65–68.
- 16 B. Schulz, M. G. Mazza and C. Bahr, *Phys. Rev. E: Stat., Nonlinear, Soft Matter Phys.*, 2014, **90**, 040501(R).